Article

Strain control of hybridization between dark and localized excitons in a 2D semiconductor

Pablo Hernández López [1,4] ✉, **Sebastian Heeg** [1,4] ✉, **Christoph Schattauer**[2], **Sviatoslav Kovalchuk** [3], **Abhijeet Kumar**[3], **Douglas J. Bock**[3], **Jan N. Kirchhof** [3], **Bianca Höfer**[3], **Kyrylo Greben** [3], **Denis Yagodkin** [3], **Lukas Linhart**[2], **Florian Libisch** [2] & **Kirill I. Bolotin** [3] ✉

Mechanical strain is a powerful tuning knob for excitons, Coulomb-bound electron–hole complexes dominating optical properties of two-dimensional semiconductors. While the strain response of bright free excitons is broadly understood, the behaviour of dark free excitons (long-lived excitations that generally do not couple to light due to spin and momentum conservation) or localized excitons related to defects remains mostly unexplored. Here, we study the strain behaviour of these fragile many-body states on pristine suspended WSe_2 kept at cryogenic temperatures. We find that under the application of strain, dark and localized excitons in monolayer WSe_2—a prototypical 2D semiconductor—are brought into energetic resonance, forming a new hybrid state that inherits the properties of the constituent species. The characteristics of the hybridized state, including an order-of-magnitude enhanced light/matter coupling, avoided-crossing energy shifts, and strain tunability of many-body interactions, are all supported by first-principles calculations. The hybridized excitons reported here may play a critical role in the operation of single quantum emitters based on WSe_2. Furthermore, the techniques we developed may be used to fingerprint unidentified excitonic states.

Excitons are responsible for the strong absorption of light by 2D transition metal dichalcogenides (TMDs)[1–3], control the valley properties of these materials[2,4,5], and condense into various correlated quantum states at low temperatures[6,7]. Most early studies focused on "bright" free excitons characterized by large oscillator strength and strong interaction with light fields. More recently, it became clear that other excitonic species may be critical for understanding and exploiting TMDs. First, "dark" excitons interact with light only weakly due to multiple selection rules and momentum conservation[8–10]. For example, the spin selection rules prohibit the radiative recombination of the ground state excitons in TMD systems such as WSe_2 or WS_2 composed of electron and hole wavefunctions in the K valley[2,8,11]. Other energetically close excitons

composed of a hole wavefunction localized in the K valley and an electron in the Q or K' valleys are dark due to the momentum selection rule. In all cases, dark excitons feature greatly increased charge lifetime, spin lifetime, and diffusion length compared to their bright counterparts[12–14]. These properties caused a surge of interest in such quasiparticles for storing and transporting quantum and classical information[15,16]. The second type of excitonic species arising in TMDs other than bright free excitons are those localized by defects. Spatially localized excitonic states are delocalized in momentum space and are thought to provide the momentum needed for energy relaxation, tunnelling, or emission from TMDs that is momentum-forbidden otherwise[17]. In addition, defect-related states function as broadly tunable quantum emitters, one

[1]Humboldt-Universität zu Berlin, Institut für Physik and IRIS Adlershof, 12489 Berlin, Germany. [2]Technische Universität Wien, 1040 Vienna, Austria. [3]Freie Universität Berlin, Department of Physics, 14195 Berlin, Germany. [4]These authors contributed equally: Pablo Hernández López, Sebastian Heeg. ✉e-mail: pablo.hernandez@physik.hu-berlin.de; sebastian.heeg@physik.hu-berlin.de; kirill.bolotin@fu-berlin.de

of the fundamental building blocks of quantum information technologies allowing the generation of entangled photons[18–23].

Applying mechanical strain changes the energies and the hierarchy of the excitonic states in TMDs. First-principles calculations reveal that different energy bands as well as the valleys within these bands experience varied rates of energy shift with strain[24,25]. Excitonic species residing in these valleys inherit the corresponding energy shifts. For example, the conduction/valence band gap at the K/K′ valleys decreases at ~100 meV/% for uniform biaxial strain[26]. Correspondingly, all excitonic species associated with these valleys including dark/bright neutral excitons, dark/bright trions, biexcitons, and their phonon replicas redshift at about the same rate. In contrast, excitons from K/Q valleys of e.g., WSe₂ have much weaker strain dependence[27,28], while localized excitons associated with defects remain primarily unaffected by strain[24,25,29]. This suggests the possibility of using the strain response signature to identify excitonic species. Even more interesting, the energy alignment between excitonic species belonging to different valleys becomes strain-dependent. As strain brings the conduction band minima at K and K′ into resonance with the localized defect states, we expect hybridization between them[13,30,31].

The arguments above show that mechanical strain engineering can be used to identify, generate, and tune novel hybridized excitonic states in TMDs. This possibility raises several questions. First, what are the properties of the hybridized states? They are generally expected to combine the traits of underlying excitons before hybridization. This is especially noteworthy in the case of the hybridization between bright defect-related localized excitons and free dark K/K′ excitons featuring high oscillator strength and long diffusion length, respectively[13,30,31]. Second, are there possible applications for the hybridized states? As strain is required for the operation of TMD-based quantum emitters, we believe that the hybridized states may be critical for the operation of these emitters and contribute to their high brightness. More broadly, the ability to manipulate the emission from long-lived dark

states may prove important for various excitonic transport devices[15]. Finally, how do we realize strain-induced hybridization experimentally? Observing well-separated peaks due to normally faint dark or localized excitonic species via optical spectroscopies requires clean, controllably strained devices operating at cryogenic temperatures. In contrast, most existing strain-engineering techniques either function at room temperature only[32–35] or do not allow in situ control of the strain level[36–40].

Here we address these questions by implementing an electrostatic-based straining approach capable of straining a pristine suspended WSe₂ monolayer at cryogenic temperatures. We identify two types of excitonic species in addition to the well-known free bright excitons: (i) the free dark excitons localized at K/K′ valleys and (ii) a pair of bright localized excitons related to shallow defects states. These two types of excitonic states have starkly different strain dependencies and are brought into energetic resonance at ~1% and ~2.5% strain (dependent on temperature). At resonance, we observe signatures of the formation of the new hybridized state, including orders-of-magnitude increased photoluminescence of dark excitons and avoided crossing behaviour between dark and localized excitonic species. Our data in combination with first-principles modelling suggests that the hybridized state combines the features of dark and localized excitons. Finally, some signatures of energetic resonance survive up to room temperature allowing us to observe pure defect emission.

Results
Model of exciton strain-dependence
In WSe₂, the low-energy physics is determined by the maxima of the valence bands and the minima of two spin-split conduction bands around the K/K′ points of the Brillouin zone, Fig. 1a. The lowest-lying excitonic states are dark (X_d^0), since the optical transition between the top of the valence band and the bottom of conduction band within one valley are prohibited by the spin selection rules, while the transition across valleys requires additional momentum. A point defect such as a
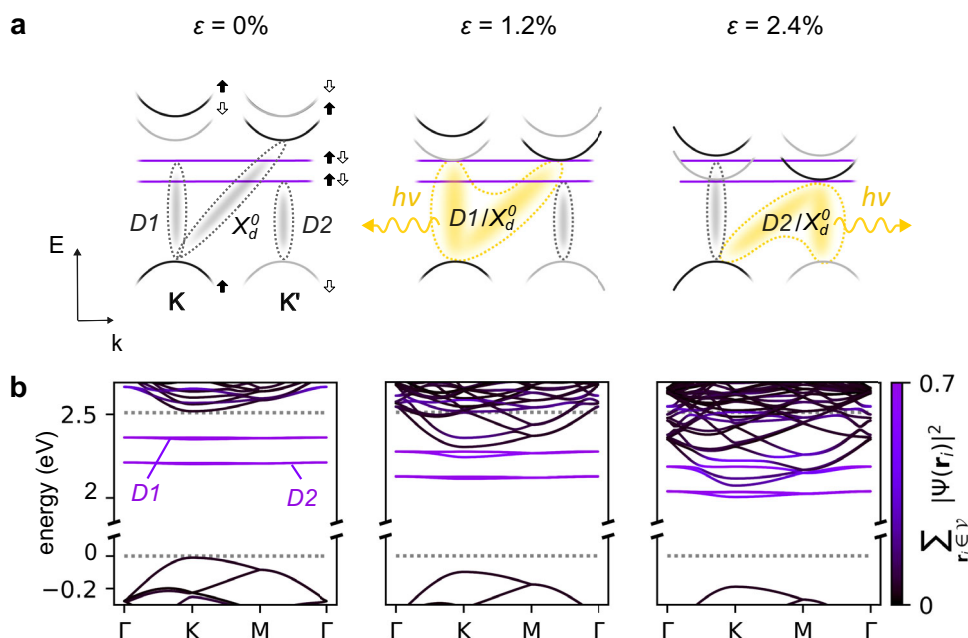

Fig. 1 | Hybridization of dark exciton and defect states. a Schematic illustration of the K and K′ valley bandstructure of WSe₂ at several different strain levels. Filled and empty arrows denote spin. **b** Corresponding bandstructure calculated via maximally localized Wannier functions generated from ab-initio calculations (see "Methods" for calculation details). The colour scale of the bands denotes their degree of localization in the immediate vicinity $\mathcal{V}$ of the defect site. Dark excitonic states X_d^0 associated with the K point become resonant with excitons related to

defect-related mid-gap states $D1$ and $D2$ at 1.2 and 2.4% strain. The energy difference between X_d^0 and $D1$, $D2$ is determined by the built-in strain in addition to externally applied strain. Since the built-in strain is temperature-dependent due to the thermal extension of involved materials as well as other effects[68], strain values at which the hybridization occurs also depend on temperature, as discussed in detail in Fig. 5.
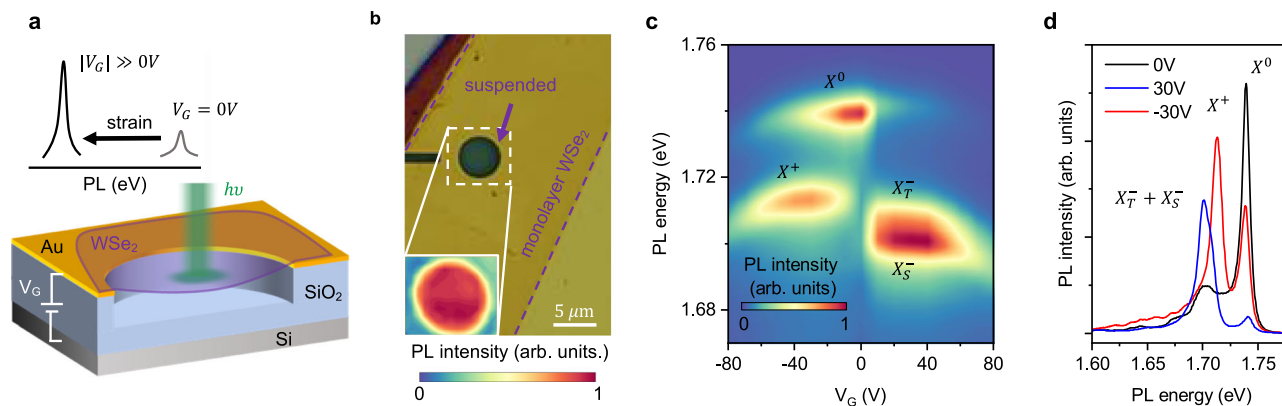
Fig. 2 | Straining suspended WSe₂ monolayers by electrostatic forces.
a Schematic of the device and measurement scheme. Applying a voltage V_G between a WSe₂ monolayer suspended over a hole and the Si backgate mechanically strains the WSe₂. We probe the strain by recording PL spectra from a small region at the centre of the suspended WSe₂ where the strain is spatially homogeneous and biaxial in nature. **b** Microscope image of a typical device. Inset: Room temperature PL map of the neutral exciton at 1.66 eV in the unstrained ($V_G = 0$V) suspended WSe₂ membrane. **c** PL spectra as a function of V_G at $T = 100$ K taken with the laser focused at the centre of the device. Selected spectra are shown in (**d**).

Neutral exciton (X^0, 1.738 eV), positively charged trion (X^+, 1.713 eV), negatively charged intervalley trion (X_T^-, 1.708 eV), and negatively charged intravalley trion (X_S^-, 1.701 eV) appear at the energies close to what is reported in literature for high-quality hBN encapsulated devices [41,43–45]. Changes in intensity and peak position for −70 V < V_G < +70 V closely resemble those in encapsulated devices, showing that charging dominates the device behaviour for this regime. The near-zero V_G position of the charge neutrality point and the disappearance of the X^0 peak outside of the −50 V < V_G < +10 V region confirm the good optical quality of our samples.

Se vacancy in WSe₂ features two strongly localized (spin-degenerate) defect states ($D1$ and $D2$) within the band gap [30,31], slightly below the conduction band minimum. The wavefunctions of excitons associated with these states are largely formed from the valence band hole and an electron localized at the selenium vacancy (Fig. 1b). As the defect breaks translational invariance, radiative recombination of $D1$, $D2$ excitons is allowed. Despite the large resulting dipole matrix element, the density of isolated defect states is low. Because of that, neither defect states nor the lowest-lying excitons provide strong photoluminescence in unstrained WSe₂.

This situation changes drastically upon the introduction of strain due to contrasting strain responses of the states X_d^0 and $D1$, $D2$[30]. In line with previous literature[27,28] our calculations show that while the conduction band at the K and K′ minima strongly downshifts with strain, the energy difference of both the valence band and the defect states remains almost constant (i.e., valence and defect bands shift at an identical, smaller rate, see Fig. 1b). Therefore, the dark exciton X_d^0 composed of conduction and valence band Bloch states exhibits a much stronger strain response compared to defect-related excitons $D1$, $D2$. As a result, X_d^0 becomes energy-degenerate with $D1$ at ~1% and with $D2$ at ~2.5% strain (Fig. 1b, top). Following Fermi's golden rule, we evaluate the dipole transition matrix element—including contributions from both valleys—to estimate the resulting photoluminescence signal from an optical decay of the different possible excitonic states (see Supplementary Note 2 for technical details). We find that at resonance conditions, the oscillator strength of the dark state X_d^0 increases by several orders of magnitude. We interpret this striking increase in the oscillator strength as the result of hybridization between dark and defect-related excitons. The hybridized state inherits the bright character of the defect exciton, allowing an efficient de-excitation channel for dark excitons. These theoretical findings imply the possibility of continuously tuning the hybridization between excitonic species as well as their oscillator strength using strain. These phenomena are largely unstudied experimentally mainly due to the difficulties associated with reaching high values of mechanical strain at cryogenic temperatures.

Straining approach

We solve the challenges associated with the application of controlled uniform strain to a high-quality WSe₂ device at low temperature by using an electrostatic straining approach. In our technique, the strain is generated by applying a gate voltage V_G between a suspended monolayer WSe₂ membrane and an electrode below, Fig. 2a. This approach combines several key advantages. First, electrostatic straining functions at cryogenic temperatures, unlike other straining approaches based on, e.g., bending elastic substrates or pressurizing a 2D membrane with gas that only work near room temperature[33–35]. Second, the approach is capable of large strain values up to a few percent, higher than the limits of other techniques[32,39]. Such high strain is necessary to reach and surpass the predicted regime in which hybridization between different excitonic species occurs. Third, suspended 2D materials are not affected by substrate-related scattering and therefore feature high optical quality necessary to resolve closely-spaced excitonic states[41–44]. The main complication associated with using electrostatic forces for straining is that the carrier density inside the device changes together with the strain level. Therefore, a careful analysis disentangling the effects of doping and strain is required (see Supplementary Fig. 2).

Quantitatively, we describe the carrier density n and strain level ε induced in our device in response to gating via

$$n = C_G V_G + n_0, \tag{1}$$

$$\varepsilon \approx \begin{cases} \alpha V_G^4 + \varepsilon_0, & \alpha V_G^4 \ll \varepsilon_0 \\ \beta V_G^{4/3}, & \alpha V_G^4 \gg \varepsilon_0 \end{cases}. \tag{2}$$

Here C_G is the gate capacitance of the device, α, β are constants dependent on device geometry, ε_0 and n_0 are built-in strain and charge doping, respectively (mechanical details in Supplementary Fig. 8). These equations show that when the gate voltage is low, $|V_G| < (\varepsilon_0/\alpha)^{1/4} \sim 100$ V in a typical device, it mostly controls the carrier density while leaving the strain nearly constant. At large $|V_G|$, mechanical strain starts to change rapidly, while being symmetric with respect to the sign of V_G.

To realize the straining geometry described above experimentally, we suspend a WSe₂ monolayer on top of a circular hole etched into an Au/SiO₂/Si substrate (Fig. 2a, b). The device is loaded into an optical cryostat and measured via photoluminescence (PL) spectroscopy (see "Methods" for details). To establish the quality of our device
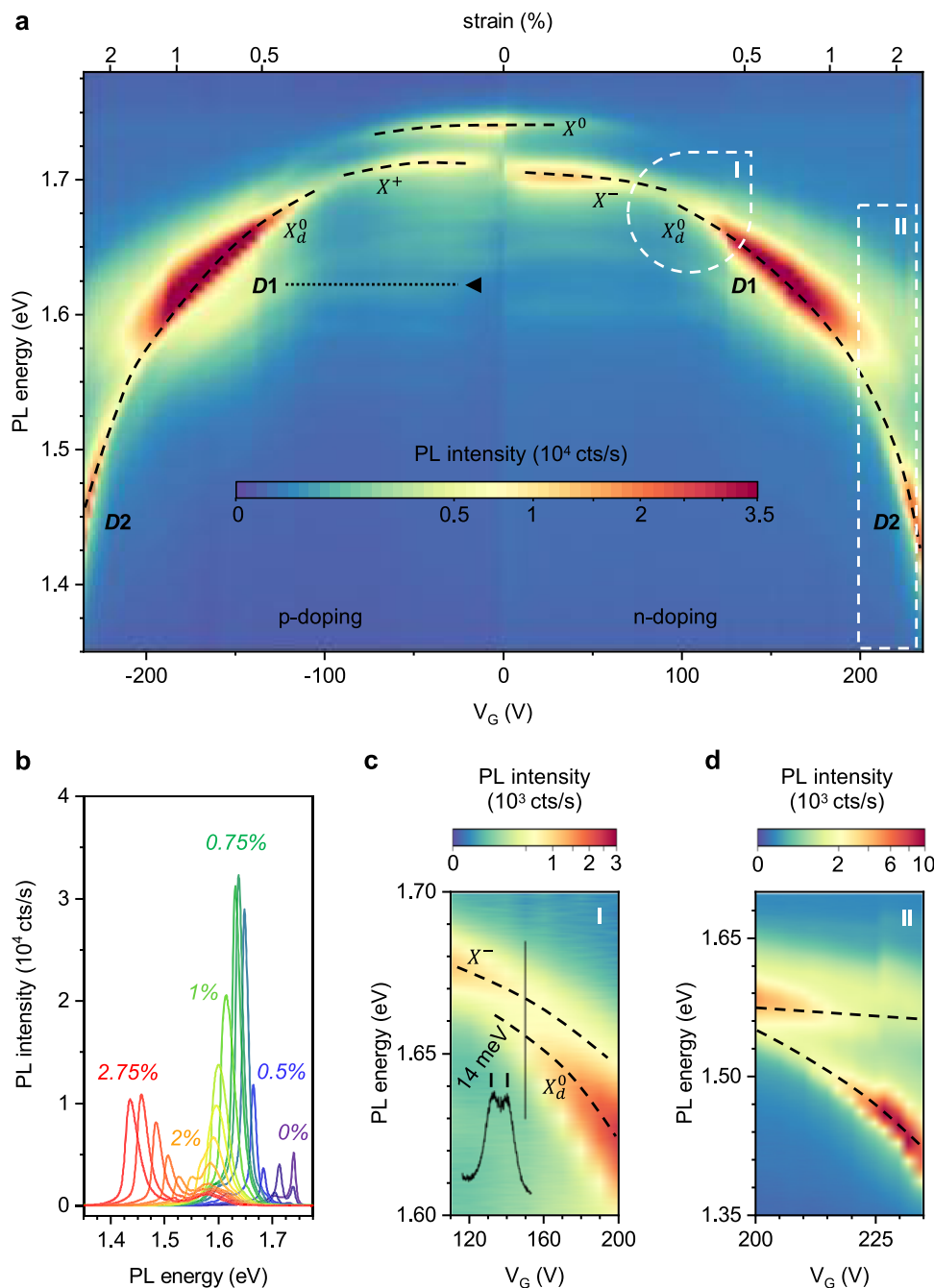
Fig. 3 | Strain response of excitonic states in WSe$_2$ at 100 K. a PL spectra map of a suspended WSe$_2$ monolayer (device 1) at $T = 100$ K with individual spectra shown in (**b**). Free excitonic states X^0, $X^{+/-}$, X_d^0 red-shift with increasing strain (the dashed lines are a guide to the eye). The state X_d^0 develops strong intensity maxima at energies 1.63 eV (*D*1) and 1.45 eV (*D*2). The strain-independent states close to the position of *D*1 that we associate with defects are marked with dashed lines.

See Supplementary Fig. 1 for an offset plot of the PL spectra. **c** High-resolution map of the region "I" from another device (device 2). The state X^- disappears with increasing strain while the state X_d^0 arises ~ 14 meV below it. **d** Detailed map of the region "II" from device 1 showing a maximum near ~ 1.4 eV and an avoided-crossing pattern.

and to identify the excitonic species, we start by exploring the low gate voltage regime $|V_G| < 80$ V, where changes in the carrier density dominate the optical response of WSe$_2$. For now, we focus on a temperature of 100 K where only the most intense excitons are visible and examine lower and higher temperatures later. Figure 2c,d shows a PL spectral map and spectra at three selected V_G. We observe narrow PL peaks corresponding to neutral exciton (X^0) and charged trions (X^+, X_T^-, X_S^-) at energies close to reported values[41,43–45]. The X^0 peak width of 7.5 meV is close to the 4–6 meV reported at $T < 5$ K for high-quality WSe$_2$ encapsulated in hBN samples[41,46].

Strain dependence of excitonic peaks

We now examine the behaviour of our suspended WSe$_2$ in the high voltage regime $|V_G| > 80$ V, where strain effects become dominant. Figure 3a shows the evolution of PL spectra taken with gate voltages up to $V_G = \pm 230$V with individual spectra shown in Fig. 3b. We observe a redshift in the energetic position of the excitons X^0, X^-, X^+ with increasing gate voltage. The redshift is equal for both polarities of V_G. This behaviour is a well-characterized effect of mechanical strain[34,42,47]. In general, uniform biaxial strain in WSe$_2$ (see "Methods" discussing this approximation) results in a downshift of all excitonic peaks at a
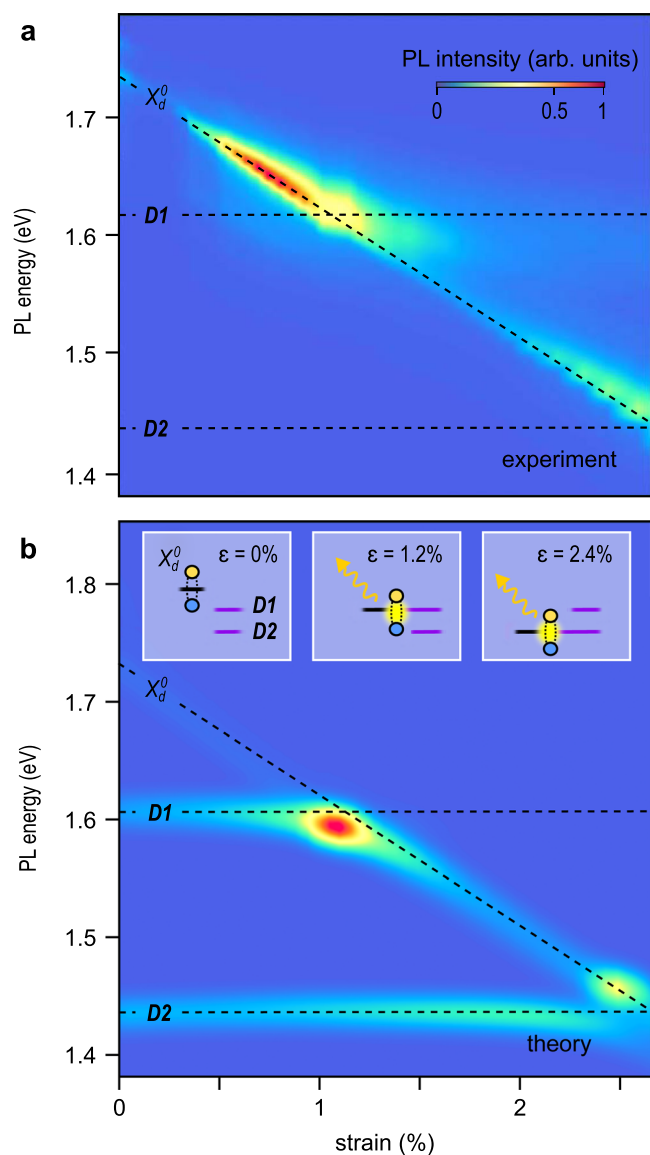
Fig. 4 | Strain-related hybridized states: comparing experiment and theory.
Experimental (**a**) and modelled (**b**) PL spectra map of WSe$_2$ vs. strain. Different shift
rates vs. strain for the defect-related states $D1, D2$ and a dark excitonic state X_d^0 are
evident. When X_d^0 is energy resonant with either $D1$ (around ε ~ 1.2%) or $D2$ (around
ε ~ 2.4%) a strong increase in oscillator strength and avoided-crossing type beha-
viours are seen. Insets show on- and off- resonant alignment between dark- and
defect-related excitons. See Supplementary Note 1 for the discussion of the dif-
ferences between the experiment and theory.

rate of 100 meV/ %. We use this value to fit the observed peak shifts to
Eq. ([2](#)) and extract the effective 2D Young's modulus of 100 N/m, close
to previously reported values[42]. We reach strain values of almost 3% in
our suspended WSe$_2$ devices[25].

We now focus on several trends in Fig. 3a, b that are not expected
from a simple model based on Eqs. ([1](#) & [2](#)) that only considers spectral
redshift due to strain and gating-related redistribution of the oscillator
strength between trions and neutral excitons. Our first and most
striking observation is the highly non-monotonic evolution of the PL
intensity with increasing strain. After the initial intensity drop, c.f.
Fig. 3a, the PL intensity increases to reach a maximum labelled $D1$ at
$V_G = \pm 160$ V (~0.7% strain) and 1.63 eV, where the integrated PL inten-
sity is a factor 6 higher than the combined intensities of neutral exci-
tons and trion for $V_G = 0$ V. It then drops and peaks again with a

maximum (labelled $D2$) at $V_G = \pm 230$ V (~2.5%), with the peak position at
1.45 eV. The state associated with greatly increased PL intensity
emerges 14 meV below the trion state as the trion gradually disappears
(Fig. 3c) and dominates the PL when it approaches the energies of $D1$
and $D2$. From its energy position, we identify ("Methods") the state as a
dark exciton, X_d^{0}[48]. Note that the energetic proximity between dark
exciton and trion requires high resolution measurements to resolve
the two peaks.

Next, in the region $|V_G| < 100 V$ we observe faint lines around 1.6 eV
that are largely strain-independent (Fig. 3a, triangles), unlike other
brighter excitonic peaks. In addition, these lines exhibit a saturating
power dependence that contrasts with the near-linear dependence for
neutral excitons and trions (see Supplementary Fig. 3). The saturating
power behaviour is characteristic of defect-related states[17,49,50]. The
near strain-independence suggests that the states do not involve Bloch
states in the conduction band (Fig. 1). Finally, the comparison of the
energy position of one of these states with our tight-binding calcula-
tions allows to unambiguously associate the state with the $D1$ exciton.
Critically, the strain-independent $D1$ exciton becomes energetically
degenerate with the downshifting state X_d^0 at about 1% strain. The first
observed PL maximum happens close to this strain value. Further-
more, the second maximum observed in PL occurs when the dark
exciton is at resonance with the state $D2$ predicted from theory, at
~2.5% strain.

Comparison with theory
Summarizing our discussion so far, the observed strong increase in
photoluminescence occurs when a strain-related modification of the
energy spectrum brings the dark exciton X_d^0 into an energetic reso-
nance with defect-related states $D1, D2$. This behaviour is especially
striking since all of these states are either very faint or invisible in
unstrained devices. The only explanation consistent with the data in
Fig. 3, including changes in the intensity and the appearance of new
spectral features, is strain-related hybridization between the dark
exciton X_d^0 and defect-related states $D1$ and $D2$, as predicted by our
tight-binding model. In Fig. 4, we directly compare the experimental
data, now plotted as a function of strain (calculated from the shift of
the excitonic peaks, see "Methods"), to the theoretical modelling. All of
the features of the above model are evident in our data, including the
linear shift of X_d^0 with strain, near strain-independence of $D1, D2$, and
an order of magnitude increase in PL intensity when X_d^0 into resonance
with $D1$ or $D2$. To confirm our interpretation, we have scrutinized other
confounding phenomena that may contribute to our data such as
strain-dependent scattering between K- and Q-valleys[25,42] or inter-
ference effects, but find that none of these effects can explain our
experimental observation (see Supplementary Note 1 and Supple-
mentary Fig. 9).

Temperature-dependent data
Having understood the strain-dependent hybridization between
dark free and bright defect-related excitons, we now want to elu-
cidate the nature of the states undergoing hybridization. For this,
we turn to more complex data at temperatures between 10 and
300 K (Fig. 5). First, the strain tunability of the excitonic states (as
quantified by their energy shift within our full voltage range)
decreases at low temperatures. At $V_G = 200$ V, we generate 2.2%
strain at 300 K and only 0.9% at 10 K. This difference is related to
temperature-dependent changes in the built-in strain and
mechanical constants of WSe$_2$[51,52]. Second, the strong enhancement
in the PL intensity occurs at roughly constant energy for $T = 10, 100$,
and 300 K (dashed lines in Fig. 5) despite a strong temperature-
dependent blueshift in the unstrained X^0 and $X^{+/-}$ excitonic peaks
with decreasing T. As discussed earlier, this behaviour is consistent
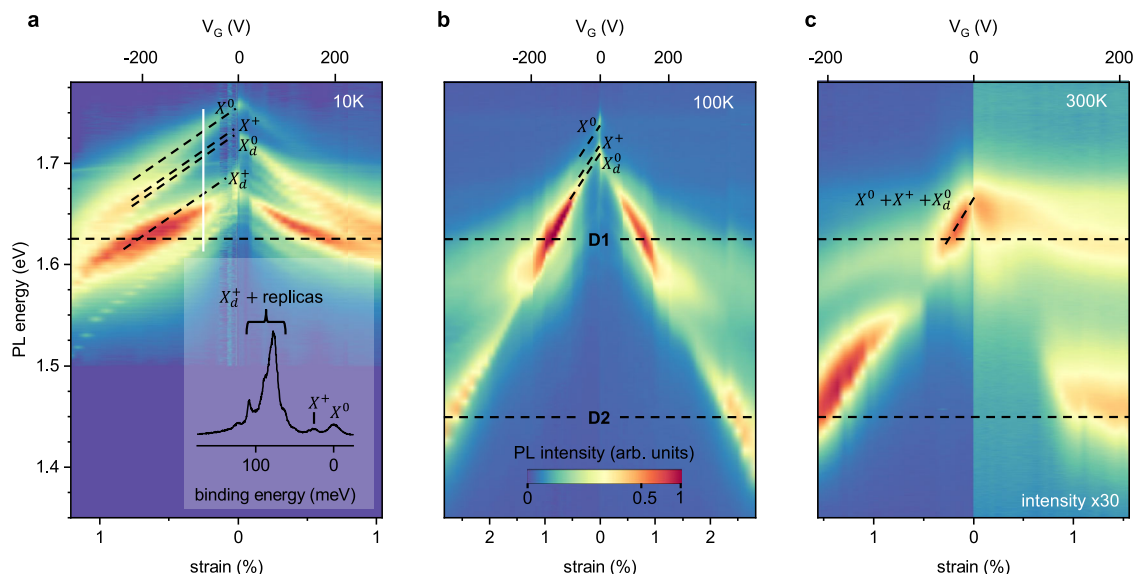with near strain-independence of defect-related excitons $D1$
and $D2$.

Fig. 5 | Temperature-dependent strain response. PL spectra vs. strain maps acquired at (**a**) $T = 10$ K, **b** 100 K, **c** 300 K. An individual spectrum at 10 K measured under 0.25% strain (−140 V) and marked with a white, solid line is shown in the inset of (**a**). While the energy of the unstrained, free excitonic states (X^0, X^+, X_d^0, the corresponding spectral lines are marked with dashed lines) blueshifts with lowering temperature, the features $D1$ and $D2$ associated with the corresponding defects stay roughly energy-independent. Due to the temperature-related changes in mechanical constants, only the $D1$ state is resolved at 10 K within our accessible V_G range. In contrast, we resolve the hybridization with both states $D1$ and $D2$ at 100 and 300 K. As opposed to the $T = 10$ K data in (**a**) that is symmetric with respect to p- and n-doping, the intensity of the n-branch at 300 K in (**c**) is roughly 30 times lower than that for the p-branch. Note that the voltage scales in (**a**–**c**) are not linear.

Third, while at 100 and 300 K the state that dominates the photoluminescence after hybridization with either $D1$ or $D2$ matches the energy position of X_d^0, we observe a more complex behaviour at 10 K, Fig. 5a (see Supplementary Fig. 4 for individual spectra). A state that lies ~80 meV (~87 meV) below X^0 for p- (n-) doping dominates the spectrum. This state is faint at zero strain, redshifts at the same rate as other excitonic states when the strain is increased, and its intensity reaches a maximum when it is brought into resonance with the defect-related state $D1$. The energy position of that state is within a band of states related to dark trions X_d^+, X_d^- and their phonon replicas [41,53]. We, therefore, suggest that at low temperatures the strain-driven hybridization between dark trions X_d^+, X_d^- on one hand and the defect state $D1$, on the other hand, dominates the emission in our devices. The fact that such a behaviour is seen only at low temperature is likely due to the increased population of dark trions at low temperatures[54].

Finally, at 300 K we see a pronounced asymmetry between positive and negative voltages both in the intensity and structure of the PL spectrum, Fig. 5c, that is in contrast to the behaviour at 10 and 100 K (see Supplementary Fig. 5 for other temperatures). As the level of strain in our experimental geometry is independent of the sign of V_G, this asymmetry must arise from changes in the carrier density. For the n-side, the PL intensity of the n-side is about 30 times lower than on the p-side and we do not see any features associated with free excitons with linear strain dependence. We only observe weakly dispersing features at the energies of states $D1$, $D2$ that do not seem to undergo hybridization. We speculate that this behaviour may be related to the small oscillator strength of free excitons seen at room temperature for substrate-supported WSe$_2$ samples for n-doping[55–57]. We, therefore, suggest that the features seen on the n-side are the intrinsic contributions from $D1$ and $D2$ localized defect states that are not masked by other much stronger excitons.

Discussion
To summarize, we show that mechanical strain brings dark- and localized defect-states into resonance. When that happens, a new hybridized state with large oscillator strength is formed. That state dominates light/matter interactions in WSe$_2$. We note that the scenario we outline can in principle occur between any pair of excitonic states that have different strain dependencies, including KK and KQ excitons[25]. Point defects other than the Se vacancies discussed here can also be involved, as long as they feature localized defect states sufficiently close to the conduction band edge to result in strain-induced hybridization. Several interesting conclusions can be drawn from our data. First, the hybridized state we observe is likely key for the operation of single quantum emitters in WSe$_2$. In these devices, highly non-uniform mechanical strain is induced in WSe$_2$ deposited onto e.g., a bed of pillars. At the point of highest strain, at the pillar's top, the hybridization conditions are fulfilled and dark excitons effectively release their energy as photons. Around the pillars' top, the strain gradient "funnels" all excitonic species, including dark, towards the point of highest strain. Since the lifetime of dark excitons is much longer than that of their bright cousins, our work shows that the area from which this funneling process "collects" the energy is much larger than what was thought previously. It is also worth noting that the processes studied here may be contributing to strain-related changes in the PL intensity previously observed in WSe$_2$ at room temperature[42]. Similar processes may happen in other TMD materials, especially in WS$_2$, where the ground state is also dark[58]. Second, our results suggest the use of mechanical strain to fingerprint excitonic complexes in TMDs. The data of Fig. 3, for example, shows that free and some defect-related excitons respond to strain very differently allowing their unambiguous identification. Finally, in the future, it will be attractive to use strain engineering to "encode" charge- or spin- information into dark excitons, towards concepts such as excitonic transistors or switches.

Methods
Sample fabrication and measurements
All devices are fabricated by transferring[59] mechanically exfoliated WSe$_2$ monolayers onto a circular hole (diameter ~ 5 μm) etched 700 nm into Au/Cr/SiO$_2$/Si (70 nm/3 nm/1500 nm/300 μm) substrates (see Supplementary Fig. 10). The large thickness of SiO$_2$ allows applying voltages of up to ±280 V before the dielectric rupture of the sample, but measurements are typically limited to ±235 V for sample protection. The monolayers are many times larger than the hole to ensure

device stability. Room temperature PL mapping of the finished device (Fig. 2b, inset) is used to confirm that the monolayer uniformly covers the hole area. The devices are measured in vacuum inside a cryostat with the base temperature of 4 K. To avoid damage to the suspended WSe_2 during pump-down of the cryostat, a pressure relief channel is fabricated in SiO_2. Temperature at the sample is detected via an on-sample temperature sensor and confirmed by tracking the energetic blueshift and linewidth narrowing of the (bright) neutral exciton (Supplementary Fig. 5). Photoluminescence measurements are carried out in a homebuilt setup using a tightly focused laser (diameter ~ 1 μm) placed at the centre of the device. We excite the membranes with a linearly polarized, CW laser with $\lambda = 532$ nm and power ~10 μW (power density 500 W/cm²) and in the range 100 nW–4.5 μW to quantify the character of excitonic states (power densities 5–250 W/cm²). Additionally, from power-dependent measurements we estimate the defect concentration on our samples to be in the order of 10^{10} cm⁻¹ (see Supplementary Fig. 3)[60]. Photoluminescence excitation spectroscopy in the range 570–675 nm with a pulsed laser source (femtosecond Ti:Sa Chameleon Ultra II + OPO-VIS) is used to quantify the contribution of interference effects in our data. The strain generated by applying a gate voltage between suspended WSe_2 and Si is largely uniform, as confirmed by modelling PL linescans across the device (see Supplementary Fig. 6), and high sharpness of excitonic features in strained devices. We ascribe strain values to each spectrum by measuring energetic shifts for excitonic species and assuming the shift rate 95 meV/%[61] for all free excitons. This analysis is confirmed through separate interferometric measurements capable of directly measuring membrane displacement with nanometre resolution (see Supplementary Fig. 7). To identify excitonic species in our PL data, we compare their energy position and the binding energy (measured with respect to the X_0 position) with detailed measurement of excitonic species in high-quality unstrained devices encapsulated in hBN[41,44,62,63]. While the difference in electrostatic screening between suspended and encapsulated devices leads to noticeable changes in the binding energy of the excitons, in most cases the identification is possible.

First-principles calculations

We perform fully spin-polarized (non-collinear), structural and electronic optimization of the pristine cell with the DFT software package VASP[64–67]. Our calculations use the Perdew-Burke-Ernzerhof (PBE) functional, include 35 Å vacuum perpendicular to the membrane and a $25 \times 25 \times 1$ Monkhorst-Pack k-space grid. Plane wave energy cutoff is set to 500 eV and the systems are electronically converged to $\delta E \approx 10^{-9}$ eV. We find an energetically favourable lattice constant of $a_0 = 3.322$ Å. We then generate TB parameters based on maximally localized Wannier functions (MLWFs) from a set of DFT calculations of the pristine system and carefully interpolate TB parametrizations for intermediate strain values. Within tight-binding, we build a 17×17 supercell, remove a single Se atom, and then calculate Bloch states. We evaluate optical transition amplitudes based on the dipole operator also taken from DFT (see Supplementary Note 2 for technical details).

Data availability

The data that support the findings of this study are available from the authors on reasonable request.

References

1. Mak, K. F., Lee, C., Hone, J., Shan, J. & Heinz, T. F. Atomically thin MoS₂: a new direct-gap semiconductor. *Phys. Rev. Lett.* **105**, 136805 (2010).
2. Wang, G. et al. Colloquium: excitons in atomically thin transition metal dichalcogenides. *Rev. Mod. Phys.* **90**, 021001 (2018).
3. Wang, Q. H., Kalantar-Zadeh, K., Kis, A., Coleman, J. N. & Strano, M. S. Electronics and optoelectronics of two-dimensional transition metal dichalcogenides. *Nat. Nanotechnol.* **7**, 699–712 (2012).
4. Manzeli, S., Ovchinnikov, D., Pasquier, D., Yazyev, O. V. & Kis, A. 2d transition metal dichalcogenides. *Nat. Rev. Mater.* **2**, 17033 (2017).
5. Schaibley, J. R. et al. Valleytronics in 2d materials. *Nat. Rev. Mater.* **1**, 16055 (2016).
6. Wang, Z. et al. Evidence of high-temperature exciton condensation in two-dimensional atomic double layers. *Nature* **574**, 76–80 (2019).
7. Andrei, E. Y. et al. The marvels of moiré materials. *Nat. Rev. Mater.* **6**, 201–206 (2021).
8. Malic, E. et al. Dark excitons in transition metal dichalcogenides. *Phys. Rev. Mater.* **2**, 014002 (2018).
9. Zhou, Y. et al. Probing dark excitons in atomically thin semi-conductors via near-field coupling to surface plasmon polaritons. *Nat. Nanotechnol.* **12**, 856–860 (2017).
10. Li, Z. et al. Direct observation of gate-tunable dark trions in monolayer WSe₂. *Nano Lett.* **19**, 6886–6893 (2019).
11. Zhang, X.-X., You, Y., Zhao, S. Y. F. & Heinz, T. F. Experimental evidence for dark excitons in monolayer WSe₂. *Phys. Rev. Lett.* **115**, 257403 (2015).
12. Zhang, X.-X. et al. Magnetic brightening and control of dark excitons in monolayer WSe₂. *Nat. Nanotechnol.* **12**, 883–888 (2017).
13. Robert, C. et al. Fine structure and lifetime of dark excitons in transition metal dichalcogenide monolayers. *Phys. Rev. B* **96**, 155423 (2017).
14. Erkensten, D. et al. Dark exciton-exciton annihilation in monolayer WSe₂. *Phys. Rev. B* **104**, l241406 (2021).
15. Tang, Y., Mak, K. F. & Shan, J. Long valley lifetime of dark excitons in single-layer WSe₂. *Nat. Commun.* **10**, 4047 (2019).
16. Mapara, V. et al. Bright and dark exciton coherent coupling and hybridization enabled by external magnetic fields. *Nano Lett.* **22**, 1680–1687 (2022).
17. Wu, Z. & Ni, Z. Spectroscopic investigation of defects in two-dimensional materials. *Nanophotonics* **6**, 1219–1237 (2017).
18. Toth, M. & Aharonovich, I. Single photon sources in atomically thin materials. *Annu. Rev. Phys. Chem.* **70**, 123–142 (2019).
19. Wehner, S., Elkouss, D. & Hanson, R. Quantum internet: a vision for the road ahead. *Science* **362**, eaam9288 (2018).
20. Atatüre, M., Englund, D., Vamivakas, N., Lee, S.-Y. & Wrachtrup, J. Material platforms for spin-based photonic quantum technologies. *Nat. Rev. Mater.* **3**, 38–51 (2018).
21. Baek, H. et al. Highly energy-tunable quantum light from moiré-trapped excitons. *Sci. Adv.* **6**, eaba8526 (2020).
22. Turunen, M. et al. Quantum photonics with layered 2d materials. *Nat. Rev. Phys.* **4**, 219–236 (2022).
23. Dastidar, M. G., Thekkooden, I., Nayak, P. K. & Bhallamudi, V. P. Quantum emitters and detectors based on 2d van der Waals materials. *Nanoscale* **14**, 5289–5313 (2022).
24. Zhang, C. et al. Probing critical point energies of transition metal dichalcogenides: surprising indirect gap of single layer WSe₂. *Nano Lett.* **15**, 6494–6500 (2015).
25. Aslan, O. B., Deng, M. & Heinz, T. F. Strain tuning of excitons in monolayer WSe₂. *Phys. Rev. B* **98**, 115308 (2018).
26. Lloyd, D. et al. Band gap engineering with ultralarge biaxial strains in suspended monolayer MoS₂. *Nano Lett.* **16**, 5836–5841 (2016).
27. Deilmann, T. & Thygesen, K. S. Finite-momentum exciton landscape in mono- and bilayer transition metal dichalcogenides. *2D Mater.* **6**, 035003 (2019).
28. Shi, H., Pan, H., Zhang, Y.-W. & Yakobson, B. I. Quasiparticle band structures and optical properties of strained monolayer MoS₂ and WS₂. *Phys. Rev. B* **87**, 155304 (2013).
29. Khatibi, Z. et al. Impact of strain on the excitonic linewidth in transition metal dichalcogenides. *2D Mater.* **6**, 015015 (2018).
30. Linhart, L. et al. Localized intervalley defect excitons as single-photon emitters in WSe₂. *Phys. Rev. Lett.* **123**, 146401 (2019).

31. Yang, D., Fan, X., Zhang, F., Hu, Y. & Luo, Z. Electronic and magnetic properties of defected monolayer WSe_2 with vacancies. *Nanoscale Res. Lett.* **14**, 192 (2019).

32. Yang, S., Chen, Y. & Jiang, C. Strain engineering of two-dimensional materials: methods, properties, and applications. *InfoMat* **3**, 397–420 (2021).

33. He, K., Poole, C., Mak, K. F. & Shan, J. Experimental demonstration of continuous electronic structure tuning via strain in atomically thin MoS_2. *Nano Lett.* **13**, 2931–2936 (2013).

34. Kovalchuk, S. et al. Neutral and charged excitons interplay in non-uniformly strain-engineered WS_2. *2D Mater.* **7**, 035024 (2020).

35. Harats, M. G., Kirchhof, J. N., Qiao, M., Greben, K. & Bolotin, K. I. Dynamics and efficient conversion of excitons to trions in non-uniformly strained monolayer WS_2. *Nat. Photonics* **14**, 324–329 (2020).

36. Lee, J.-K. et al. Modification of electrical properties of graphene by substrate-induced nanomodulation. *Nano Lett.* **13**, 3494–3500 (2013).

37. Gill, S. T. et al. Mechanical control of graphene on engineered pyramidal strain arrays. *ACS Nano* **9**, 5799–5806 (2015).

38. Khestanova, E., Guinea, F., Fumagalli, L., Geim, A. K. & Grigorieva, I. V. Universal shape and pressure inside bubbles appearing in van der Waals heterostructures. *Nat. Commun.* **7**, 12587 (2016).

39. Branny, A., Kumar, S., Proux, R. & Gerardot, B. D. Deterministic strain-induced arrays of quantum emitters in a two-dimensional semiconductor. *Nat. Commun.* **8**, 15053 (2017).

40. Parto, K., Azzam, S. I., Banerjee, K. & Moody, G. Defect and strain engineering of monolayer WSe_2 enables site-controlled single-photon emission up to 150k. *Nat. Commun.* **12**, 3585 (2021).

41. Rivera, P. et al. Intrinsic donor-bound excitons in ultraclean monolayer semiconductors. *Nat. Commun.* **12**, 871 (2021).

42. Aslan, B. et al. Excitons in strained and suspended monolayer WSe_2. *2D Mater.* **9**, 015002 (2021).

43. He, M. et al. Valley phonons and exciton complexes in a monolayer semiconductor. *Nat. Commun.* **11**, 618 (2020).

44. Liu, E. et al. Multipath optical recombination of intervalley dark excitons and trions in monolayer WSe_2. *Phys. Rev. Lett.* **124**, 196802 (2020).

45. Kirchhof, J. N. et al. Nanomechanical spectroscopy of 2d materials. *Nano Lett.* https://doi.org/10.1021/acs.nanolett.2c01289 (2022).

46. Liu, E. et al. Gate tunable dark trions in monolayer WSe_2. *Phys. Rev. Lett.* **123**, 027401 (2019).

47. Conley, H. J. et al. Bandgap engineering of strained monolayer and bilayer MoS_2. *Nano Lett.* **13**, 3626–3630 (2013).

48. Noori, K., Cheng, N. L. Q., Xuan, F. & Quek, S. Y. Dielectric screening by 2d substrates. *2D Mater.* **6**, 035036 (2019).

49. Schmidt, T., Lischka, K. & Zulehner, W. Excitation-power dependence of the near-band-edge photoluminescence of semiconductors. *Phys. Rev. B* **45**, 8989–8994 (1992).

50. Barbone, M. et al. Charge-tuneable biexciton complexes in monolayer WSe_2. *Nat. Commun.* **9**, 3721 (2018).

51. Morell, N. et al. High quality factor mechanical resonators based on WSe_2 monolayers. *Nano Lett.* **16**, 5102–5108 (2016).

52. Nicholl, R. J. et al. The effect of intrinsic crumpling on the mechanics of free-standing graphene. *Nat. Commun.* **6**, 8789 (2015).

53. Huang, J., Hoang, T. B. & Mikkelsen, M. H. Probing the origin of excitonic states in monolayer WSe_2. *Sci. Rep.* **6**, 22414 (2016).

54. Arora, A. et al. Dark trions govern the temperature-dependent optical absorption and emission of doped atomically thin semiconductors. *Phys. Rev. B* **101**, 241413 (2020).

55. Shinokita, K. et al. Continuous control and enhancement of excitonic valley polarization in monolayer wse2 by electrostatic doping. *Adv. Funct. Mater.* **29**, 1900260 (2019).

56. Ye, T. et al. Room-temperature exciton-based optoelectronic switch. *Small* **17**, 2005918 (2021).

57. Allain, A. & Kis, A. Electron and hole mobilities in single-layer WSe_2. *ACS Nano* **8**, 7180–7185 (2014).

58. Echeverry, J. P., Urbaszek, B., Amand, T., Marie, X. & Gerber, I. C. Splitting between bright and dark excitons in transition metal dichalcogenide monolayers. *Phys. Rev. B* **93**, 121107 (2016).

59. Castellanos-Gomez, A. et al. Deterministic transfer of two-dimensional materials by all-dry viscoelastic stamping. *2D Mater.* **1**, 011002 (2014).

60. Greben, K., Arora, S., Harats, M. G. & Bolotin, K. I. Intrinsic and extrinsic defect-related excitons in TMDCs. *Nano Lett.* **20**, 2544–2550 (2020).

61. Frisenda, R. et al. Biaxial strain tuning of the optical properties of single-layer transition metal dichalcogenides. *npj 2D Mater. Appl.* **1**, 10 (2017).

62. Li, Z. et al. Momentum-dark intervalley exciton in monolayer tung-sten diselenide brightened via chiral phonon. *ACS Nano* **13**, 14107–14113 (2019).

63. Liu, E. et al. Valley-selective chiral phonon replicas of dark excitons and trions in monolayer WSe_2. *Phys. Rev. Res.* **1**, 032007 (2019).

64. Kresse, G. & Furthmüller, J. Efficient iterative schemes for ab initio total-energy calculations using a plane-wave basis set. *Phys. Rev. B* **54**, 11169–11186 (1996).

65. Kresse, G. & Furthmüller, J. Efficiency of ab-initio total energy calculations for metals and semiconductors using a plane-wave basis set. *Comput. Mater. Sci.* **6**, 15–50 (1996).

66. Kresse, G. & Hafner, J. Ab initio molecular dynamics for liquid metals. *Phys. Rev. B* **47**, 558–561 (1993).

67. Kresse, G. & Hafner, J. Ab initio molecular-dynamics simulation of the liquid-metal-amorphous-semiconductor transition in germanium. *Phys. Rev. B* **49**, 14251–14269 (1994).

68. Plechinger, G. et al. Identification of excitons, trions and biexcitons in single-layer WS_2. *Phys. Status Solidi (RRL) - Rapid Res. Lett.* **9**, 457–461 (2015).

Acknowledgements

Author contributions

P.H.L. and D.J.B. fabricated the samples with support from B.H. and J.K. P.H.L., S.H., D.J.B., A.K., S.K., and D.Y. measured the PL data assisted by K.G. P.H.L., J.N.K., D.J.B., and A.K. performed reflectivity measurements. P.H.L., S.H., and K.I.B. analyzed the experimental data with support from D.J.B and A.K. L.L., C.S., and F.L. performed the DFT and TB calculations. P.H.L., S.H., C.S., F.L., and K.I.B. co-wrote the paper with input from all authors. S.H. conceived the project. K.I.B. and S.H. supervised the project.

Funding

Competing interests

The authors declare no competing interests.

Additional information

Supplementary information The online version contains supplementary material available at https://doi.org/10.1038/s41467-022-35352-9.

Correspondence and requests for materials should be addressed to Pablo Hernández López, Sebastian Heeg or Kirill I. Bolotin.

Peer review information *Nature Communications* thanks Runchen Lai and the other, anonymous, reviewer(s) for their contribution to the peer review of this work.

Reprints and permissions information is available at http://www.nature.com/reprints

Publisher's note Springer Nature remains neutral with regard to jurisdictional claims in published maps and institutional affiliations.